Multi-Functional Non-Orthogonal AFDM Waveform for Integrated Sensing and Communications

Qin Yi, Ping Yang, Senior Member, IEEE, Zilong Liu, Senior Member, IEEE, Yue Xiao, Member, IEEE, Agata Manolova, Member, IEEE, Vladimir Poulkov, Senior Member, IEEE, and Gang Wu, Senior Member, IEEE

Abstract—This paper proposes a novel multi-functional non-orthogonal affine frequency division multiplexing (nAFDM)-based integrated sensing and communications (ISAC) framework. From the communication aspect, a K-Best sphere decoding detector is developed by exploiting the affine frequency-domain noise covariance matrix, enabling efficient symbol detection with controllable search complexity. For sensing, the delay- and Doppler-dependent phase rotations of the received echo signal are analyzed, based on which low-complexity two-dimensional fast Fourier transform-based processing is employed for range and velocity estimation. Furthermore, the corresponding range and velocity resolutions, together with the maximum unambiguous range and velocity, are analytically derived, revealing the dependence of the range-related metrics on the bandwidth compression factor. Numerical results demonstrate that the proposed nAFDM-ISAC framework can flexibly balance communication and sensing requirements in terms of bit error rate (BER), effective spectral efficiency (SE), peak-to-average power ratio, and range and velocity estimation accuracy. In particular, when the bandwidth compression factor is set to 0.85, nAFDM provides an approximate effective SE gain of 17.65% over conventional AFDM, while maintaining comparable BER and sensing performance.

Index Terms—AFDM, ISAC, non-orthogonal waveform.

I. Introduction

Reliable wireless transmission in high-mobility scenarios, such as high-speed railways, vehicle-to-everything networks, unmanned aerial vehicles, and low-earth-orbit satellite systems, has become an important requirement for the upcoming sixth-generation (6G) networks and beyond [1]. In such scenarios, large Doppler shifts/spread and rapid channel variations give rise to doubly selective fading channels, under which conventional orthogonal frequency division multiplexing may suffer from severe inter-carrier interference. To address this issue, advanced waveforms such as orthogonal chirp division multiplexing (OCDM) [2] and orthogonal time frequency space (OTFS) [3] have been investigated. However, OCDM may not achieve the optimal diversity order when its chirp rate is not matched to the delay-Doppler profile of the channel, while OTFS often requires relatively high-complexity two-dimensional signal processing [4]. Recently, affine frequency division multiplexing (AFDM) has been proposed as a promising backwards-compatible waveform for resilient high-mobility communications, in which information symbols in the affine frequency (AF) domain are mapped onto a set of orthogonal chirp subcarriers via the inverse discrete affine Fourier transform [4]. Importantly, AFDM can achieve full diversity in doubly selective channels by properly configuring the chirp parameters according to the channel characteristics. Based on these favorable properties, AFDM has been extensively investigated and further extended by integrating advanced transmission paradigms to improve energy efficiency and transmission flexibility, such as index modulation [5] and discrete affine Fourier transform (DAFT)-spreading-based multiple access [6].

Beyond reliable data transmission, future wireless networks are also expected to provide accurate environmental perception capabilities, such as localization, ranging, tracking, and situational awareness [7]. Motivated by these requirements, the concept of integrated sensing and communications (ISAC) has emerged, in which a joint waveform is adopted to support both communication and sensing functionalities. In such a way, one is able to achieve higher spectral and energy efficiencies, mutual enhancement of communication and sensing, as well as lower hardware costs [8]. Recently, AFDM has been explored for ISAC applications, including target parameter estimation [9] and pilot design [10]. However, most existing works are based on conventional orthogonal AFDM, whose spectral efficiency (SE) is restricted by the orthogonality constraint among chirp subcarriers.

To further improve SE, non-orthogonal AFDM (nAFDM) was proposed as a spectrally efficient extension of AFDM by introducing a bandwidth compression factor to enable controllable non-orthogonality among chirp subcarriers [11], [12]. Existing studies on nAFDM have mainly

Copyright (c) 20xx IEEE. Personal use of this material is permitted. However, permission to use this material for any other purposes must be obtained from the IEEE by sending a request to pubs-permissions@ieee.org.

Qin Yi, Ping Yang, Yue Xiao, and Gang Wu are with the National Key Laboratory of Wireless Communications, University of Electronic Science and Technology of China, Chengdu, Sichuan 611731, China (e-mail: yiqin@std.uestc.edu.cn; yang.ping@uestc.edu.cn; xiaoyue@uestc.edu.cn; wugang99@uestc.edu.cn).

Zilong Liu is with the School of Computer Science and Electronics Engineering, University of Essex, Colchester CO4 3SQ, U.K. (e-mail: zilong.liu@essex.ac.uk).

Agata Manolova and Vladimir Poulkov are with the Faculty of Telecommunications Technical University of Sofia, 1000 Sofia, Bulgaria (amanolova@tu-sofia.bg; vkp@tu-sofia.bg).

This work was supported by the National Key R&D Program of China under Grant 2025YFE0100900, the National Key Science and Technology Major Project of China under Grant 2025ZD1302000, and the Bulgarian National Science Fund under Project BG-175467353-2024-06-0015-C01. This work is also supported by the Sichuan Provincial "Double Thousand Plan" International Joint Research and Development Program under Grant No. 2026YFHZ0314.

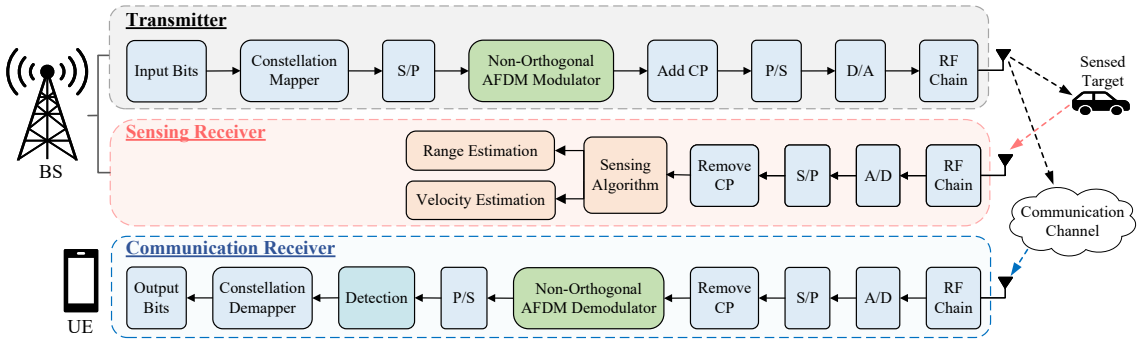

Fig. 1. Block diagram of the proposed nAFDM-ISAC system, where the signal reflected by the target is received by the sensing receiver at the base station (BS), and the signal transmitted through the downlink wireless channel is received by the communication receiver at the user equipment (UE).

focused on communication-oriented transceiver design, including zero-forcing and minimum mean square error (MMSE) precoding schemes [11], as well as linear MMSE and iterative detection algorithms [11], [12]. However, the potential of nAFDM for ISAC systems and the impact of bandwidth compression on sensing performance remain unexplored.

Against this backdrop, we propose a novel multi-functional nAFDM-ISAC framework that simultaneously supports spectrally efficient high-mobility communications and target sensing. The main contributions are summarized as follows:

- We characterize the distribution of the AF-domain noise and derive a closed-form expression for its covariance matrix. Based on this statistical characterization, a K-Best sphere decoding (SD) detector is developed for nAFDM communication reception, in which the eigenvalue decomposition of the noise covariance matrix is leveraged to transform the weighted detection metric into an equivalent Euclidean-distance form, enabling efficient tree-search detection with controllable complexity.
- We formulate the sensing signal model for nAFDM and derive its α-dependent frequency-time sensing response, in which the target delay and Doppler shift induce separable phase rotations along the frequency and time dimensions, respectively. By exploiting this frequency-time structure, a low-complexity two-dimensional fast Fourier transform (2D-FFT)-based method is adopted for range and velocity estimation, under which the corresponding range and velocity resolutions as well as the maximum unambiguous range and velocity are analytically derived. The analysis reveals that α affects the range-related metrics but not the velocity-related metrics, thereby providing an additional degree of freedom for sensing design.
- Simulation results demonstrate that 1) the proposed K-Best SD detector achieves substantial bit error rate (BER) gains over the conventional MMSE detector; 2) nAFDM provides an attractive trade-off among BER, effective SE, and peak-to-average power ratio (PAPR) compared with conventional AFDM; and 3) nAFDM incurs only a slight loss in range estimation accuracy while maintaining nearly the same velocity sensing capability as AFDM.

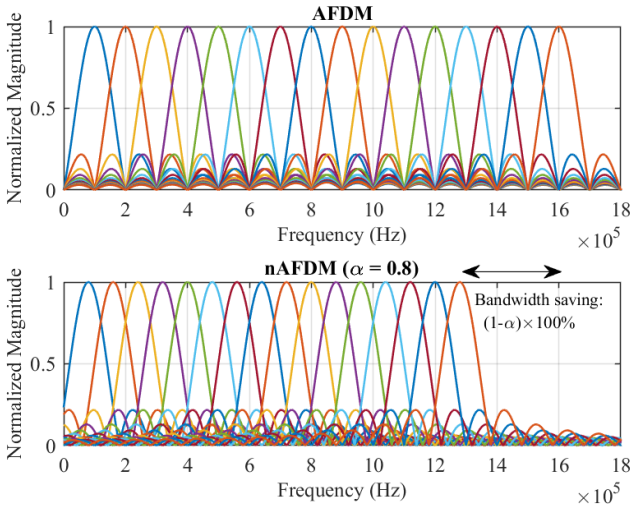

Fig. 2. Spectral comparison between conventional AFDM and nAFDM with $\alpha = 0.8$ for $N = 16$.

II. System Model

A. Transmitted nAFDM-ISAC Signal

The transceiver structure of the proposed nAFDM-ISAC system is illustrated in Fig. 1. Consider N_{sym} nAFDM symbols, each with bandwidth $B = N\Delta f$ and duration T, where N denotes the number of chirp subcarriers, $\Delta f = \alpha/T$ is the chirp subcarrier spacing, and α represents the bandwidth compression factor. We note that when $\alpha = 1$, nAFDM reduces to conventional AFDM, whereas $\alpha \in (0, 1)$ introduces controlled non-orthogonality among chirp subcarriers. Fig. 2 illustrates the spectra of chirp subcarriers for conventional AFDM and nAFDM. Compared with conventional AFDM, nAFDM occupies a narrower bandwidth, yielding a bandwidth saving of $(1 - \alpha) \times 100\%$.

Let $\mathbf{x}_m = [x_{m,0}, x_{m,1}, \ldots, x_{m,N-1}]^T \in \mathbb{C}^{N\times 1}$ denote the AF-domain information symbol vector of the mth nAFDM symbol, where $m = 0, 1, \ldots, N_{\text{sym}} - 1$. The corresponding time-domain signal is obtained via nAFDM modulation as

$$s_m[n] = \sum_{q=0}^{N-1} x_{m,q}\phi_n(q), n = 0, \ldots, N-1, \qquad (1)$$

where $\phi_n(q) = \frac{1}{\sqrt{N}} e^{\imath 2\pi\left(c_1 n^2 + c_2 q^2 + \frac{\alpha n q}{N}\right)}$, and $c_1 \geq 0$ and $c_2 \geq 0$ denote the chirp parameters. In matrix form, (1) can be expressed as $\mathbf{s}_m = \mathbf{A}_\alpha^H \mathbf{x}_m$, where $\mathbf{A}_\alpha = \mathbf{\Lambda}_{c_2} \mathbf{F}_\alpha \mathbf{\Lambda}_{c_1}$ represents the nAFDM transform matrix. Here, $\mathbf{\Lambda}_c = \text{diag}\left(e^{-\imath 2\pi c n^2}, n = 0, \ldots, N-1\right)$ for $c \in \{c_1, c_2\}$, and $\mathbf{F}_\alpha$ has entries $F_\alpha[n,q] = \frac{1}{\sqrt{N}} e^{-\imath 2\pi \alpha n q/N}$, for $n, q = 0, \ldots, N-1$. Before transmission, a cyclic prefix (CP) of length L_{CP} is appended to mitigate inter-symbol interference [12], where L_{CP} is chosen to be no smaller than the maximum channel delay spread.

B. Communication Signal Model

For communications, the transmitted nAFDM signal propagates through a doubly selective channel with P_{c} paths. The channel impulse response at time index n and delay index l of the mth nAFDM symbol can be expressed as

$$g_m(n,l) = \sum_{i=1}^{P_{\text{c}}} h_{m,i}\, e^{-\imath \frac{2\pi}{N} \nu_{m,i} n}\, \delta(l - l_{m,i}), \tag{2}$$

where $h_{m,i}$, $\nu_{m,i} \in [-\nu_{\max}, \nu_{\max}]$, and $l_{m,i} \in [0, l_{\max}]$ denote the channel gain, normalized Doppler shift, and delay shift of the ith path for the mth nAFDM symbol, respectively. Moreover, $\delta(\cdot)$ denotes the Dirac delta function, while $\nu_{\max}$ and $l_{\max}$ represent the maximum normalized Doppler shift and the maximum delay spread, respectively. Therefore, the time-domain channel matrix can be formulated as $\mathbf{H}_{\text{T},m} = \sum_{i=1}^{P_{\text{c}}} h_{m,i} \mathbf{\Delta}_{\nu_{m,i}} \mathbf{\Pi}^{l_{m,i}}$, where $\mathbf{\Delta}_{\nu_{m,i}} \triangleq \text{diag}\left(e^{-\imath \frac{2\pi}{N} \nu_{m,i} n}, n = 0, 1, \ldots, N-1\right)$, and $\mathbf{\Pi} \in \mathbb{C}^{N \times N}$ is the forward cyclic-shift matrix [4].

After discarding the CP, the time-domain received signal of the mth nAFDM symbol can be expressed as

$$\mathbf{y}_{\text{T},m} = \mathbf{H}_{\text{T},m} \mathbf{s}_m + \mathbf{n}_{\text{T},m}, \tag{3}$$

where $\mathbf{n}_{\text{T},m} \sim \mathcal{CN}(\mathbf{0}, \sigma_{\text{c}}^2 \mathbf{I}_N)$ denotes the time-domain additive white Gaussian noise (AWGN) vector, and σ_{c}^2 is the noise variance. Then, by applying nAFDM demodulation, the received signal in the AF domain can be written as

$$\mathbf{y}_{\text{AF},m} = \mathbf{A}_\alpha \mathbf{y}_{\text{T},m} = \mathbf{H}_{\text{AF},m} \mathbf{x}_m + \mathbf{n}_{\text{AF},m}, \tag{4}$$

where $\mathbf{H}_{\text{AF},m} = \mathbf{A}_\alpha \mathbf{H}_{\text{T},m} \mathbf{A}_\alpha^H$ denotes the equivalent AF-domain channel matrix, and $\mathbf{n}_{\text{AF},m} = \mathbf{A}_\alpha \mathbf{n}_{\text{T},m}$ represents the AF-domain noise vector. Since $\mathbf{A}_\alpha$ is generally non-unitary for $\alpha \in (0,1)$, $\mathbf{n}_{\text{AF},m}$ becomes colored Gaussian noise, i.e., $\mathbf{n}_{\text{AF},m} \sim \mathcal{CN}(\mathbf{0}, \sigma_{\text{c}}^2 \mathbf{C}_\alpha)$, where $\mathbf{C}_\alpha = \mathbf{A}_\alpha \mathbf{A}_\alpha^H$. Specifically, the (q_1, q_2)th entry of $\mathbf{C}_\alpha$ is given by

$$\begin{aligned} C_\alpha[q_1, q_2] &= \frac{1}{N} e^{-\imath 2\pi c_2 (q_1^2 - q_2^2)} \sum_{k=0}^{N-1} e^{-\imath \frac{2\pi}{N} \alpha (q_1 - q_2) k} \\ &= \begin{cases} 1, & q_1 = q_2, \\ \frac{1}{N} e^{-\imath 2\pi c_2 (q_1^2 - q_2^2)} \frac{1 - e^{-\imath 2\pi \alpha (q_1 - q_2)}}{1 - e^{-\imath \frac{2\pi}{N} \alpha (q_1 - q_2)}}, & q_1 \neq q_2. \end{cases} \end{aligned} \tag{5}$$

C. Sensing Signal Model

For sensing, the transmitted nAFDM waveform is reflected by P_{s} targets, each characterized by its line-of-sight path [10]. Let β_p, R_p, and v_p denote the complex reflection coefficient, range, and relative velocity of the pth target, respectively. The corresponding delay and Doppler shift are given by $\tau_p = \frac{2R_p}{c}$ and $f_{D,p} = \frac{2 v_p f_c}{c}$, where c denotes the speed of light and f_c is the carrier frequency.

After CP removal, the discrete-time echo of the mth nAFDM symbol can be written as

$$r_{\text{T},m}[n] = \sum_{p=1}^{P_{\text{s}}} \beta_p s_m[n - \iota_p]\, e^{\imath 2\pi f_{D,p} m T_{\text{sym}}} + w_{\text{T},m}[n], \tag{6}$$

where $\iota_p = \tau_p N / T$ denotes the discrete delay index of the pth target, $T_{\text{sym}} = (1 + L_{\text{CP}}/N) T$ is the nAFDM symbol interval, and $w_{\text{T},m}[n] \sim \mathcal{CN}(0, \sigma_{\text{s}}^2)$ represents the time-domain AWGN with variance σ_{s}^2.

III. Detection and Sensing Design

A. K-Best SD Detection

For notational simplicity, the nAFDM symbol index m is omitted in this subsection since detection is applied to each nAFDM symbol independently. Based on the AF-domain received signal in (4), the communication signal model can be rewritten as $\mathbf{y}_{\text{AF}} = \mathbf{H}_{\text{AF}} \mathbf{x} + \mathbf{n}_{\text{AF}}$. Accordingly, the maximum-likelihood (ML) detector can be expressed as

$$\hat{\mathbf{x}} = \arg \min_{\mathbf{x} \in \mathcal{A}^N} \mathbf{e}^H(\mathbf{x}) \mathbf{C}_\alpha^{-1} \mathbf{e}(\mathbf{x}), \tag{7}$$

where $\mathbf{e}(\mathbf{x}) = \mathbf{y}_{\text{AF}} - \mathbf{H}_{\text{AF}} \mathbf{x}$ and $\mathcal{A}$ denotes the modulation alphabet. Although (7) provides the optimal detection criterion, exhaustive ML detection requires searching over all possible symbol vectors, resulting in a complexity on the order of $\mathcal{O}\left(|\mathcal{A}|^N\right)$. To strike a balance between detection performance and computational complexity, we develop a K-Best SD detector. Specifically, the AF-domain noise covariance matrix $\mathbf{C}_\alpha$ is exploited to reformulate the weighted criterion $\mathbf{e}^H(\mathbf{x}) \mathbf{C}_\alpha^{-1} \mathbf{e}(\mathbf{x})$ into the Euclidean-distance form. Then, QR decomposition is applied to the transformed detection metric, based on which a backward breadth-first tree search is performed by retaining only a fixed number of promising candidate paths at each layer.

Since $\mathbf{C}_\alpha$ is a Hermitian matrix, it can be eigenvalue decomposed as $\mathbf{C}_\alpha = \mathbf{U}_\alpha \mathbf{\Lambda}_\alpha \mathbf{U}_\alpha^H$, where $\mathbf{U}_\alpha$ is a unitary matrix whose columns are the eigenvectors of $\mathbf{C}_\alpha$, and $\mathbf{\Lambda}_\alpha$ is a diagonal matrix containing the corresponding eigenvalues. Then, (7) can be rewritten as

$$\begin{aligned} \hat{\mathbf{x}} &= \arg \min_{\mathbf{x} \in \mathcal{A}^N} \mathbf{e}^H(\mathbf{x}) \mathbf{U}_\alpha \mathbf{\Lambda}_\alpha^{-1} \mathbf{U}_\alpha^H \mathbf{e}(\mathbf{x}) \\ &= \arg \min_{\mathbf{x} \in \mathcal{A}^N} \left[\mathbf{\Lambda}_\alpha^{-\frac{1}{2}} \mathbf{U}_\alpha^H \mathbf{e}(\mathbf{x})\right]^H \left[\mathbf{\Lambda}_\alpha^{-\frac{1}{2}} \mathbf{U}_\alpha^H \mathbf{e}(\mathbf{x})\right] \\ &= \arg \min_{\mathbf{x} \in \mathcal{A}^N} \left\| \tilde{\mathbf{y}}_{\text{AF}} - \tilde{\mathbf{H}}_{\text{AF}} \mathbf{x} \right\|^2, \end{aligned} \tag{8}$$

where $\tilde{\mathbf{y}}_{\text{AF}} = \mathbf{\Lambda}_\alpha^{-\frac{1}{2}} \mathbf{U}_\alpha^H \mathbf{y}_{\text{AF}}$ and $\tilde{\mathbf{H}}_{\text{AF}} = \mathbf{\Lambda}_\alpha^{-\frac{1}{2}} \mathbf{U}_\alpha^H \mathbf{H}_{\text{AF}}$. To efficiently solve (8), QR decomposition is performed on $\tilde{\mathbf{H}}_{\text{AF}}$ as $\tilde{\mathbf{H}}_{\text{AF}} = \mathbf{Q}\mathbf{R}$, where $\mathbf{Q}$ represents a unitary matrix and $\mathbf{R}$ is an upper triangular matrix. By defining

$\bar{\mathbf{y}} = \mathbf{Q}^H \tilde{\mathbf{y}}_{\mathrm{AF}}$, the detection metric in (8) can be further expressed as

$$\left\| \tilde{\mathbf{y}}_{\mathrm{AF}} - \tilde{\mathbf{H}}_{\mathrm{AF}} \mathbf{x} \right\|^2 = \left\| \bar{\mathbf{y}} - \mathbf{R}\mathbf{x} \right\|^2 . \tag{9}$$

Due to the upper triangular structure of $\mathbf{R}$, the metric in (9) can be evaluated through a backward tree search [13]. Let $\mathcal{L}_\kappa$ denote the surviving path set after processing the κth layer, and $\mathbf{p}_\kappa = [x_\kappa, x_{\kappa+1}, \ldots, x_{N-1}]^T$ denote a partial path from layer κ to layer $N-1$. Moreover, let $d_\kappa(\mathbf{p}_\kappa)$ denote the accumulated metric associated with $\mathbf{p}_\kappa$. The search is initialized with an empty path as $\mathcal{L}_N = \{\emptyset\}$ and $d_N(\emptyset) = 0$.

At the κth layer, for $\kappa = N-1, N-2, \ldots, 0$, each surviving path in $\mathcal{L}_{\kappa+1}$ is expanded with all possible constellation points, yielding the candidate path set

$$\mathcal{E}_\kappa = \left\{ [a, \mathbf{p}_{\kappa+1}^T]^T \mid a \in \mathcal{A},\, \mathbf{p}_{\kappa+1} \in \mathcal{L}_{\kappa+1} \right\}. \tag{10}$$

For each candidate path $\mathbf{p}_\kappa = [x_\kappa, x_{\kappa+1}, \ldots, x_{N-1}]^T \in \mathcal{E}_\kappa$, its accumulated metric is computed as

$$d_\kappa(\mathbf{p}_\kappa) = d_{\kappa+1}(\mathbf{p}_{\kappa+1}) + \left| \bar{y}_\kappa - \sum_{j=\kappa+1}^{N-1} R_{\kappa,j} x_j - R_{\kappa,\kappa} x_\kappa \right|^2 . \tag{11}$$

The surviving path set is then updated as

$$\mathcal{L}_\kappa = \mathrm{Kmin}_{\mathbf{p}_\kappa \in \mathcal{E}_\kappa} d_\kappa(\mathbf{p}_\kappa), \tag{12}$$

where $\mathrm{Kmin}(\cdot)$ returns the $\min(K_{\mathrm{SD}}, |\mathcal{E}_\kappa|)$ candidate paths with the smallest accumulated metrics, and K_{SD} denotes the tree width. After all layers are processed, the detected symbol vector is obtained by

$$\hat{\mathbf{x}} = \arg \min_{\mathbf{p}_0 \in \mathcal{L}_0} d_0(\mathbf{p}_0). \tag{13}$$

For the proposed K-Best SD detector, the eigenvalue decomposition of $\mathbf{C}_\alpha$ and the QR decomposition of $\tilde{\mathbf{H}}_{\mathrm{AF}}$ require $\mathcal{O}(N^3)$ complexity. In the tree-search stage, the recursive metric evaluation in (11) incurs $\mathcal{O}(K_{\mathrm{SD}}|\mathcal{A}|N^2)$ complexity, while candidate-path sorting contributes $\mathcal{O}(NK_{\mathrm{SD}}|\mathcal{A}|\log_2(K_{\mathrm{SD}}|\mathcal{A}|))$. Hence, the overall complexity of the proposed detector is given by $\mathcal{O}\big(N^3 + K_{\mathrm{SD}}|\mathcal{A}|N^2 + NK_{\mathrm{SD}}|\mathcal{A}|\log_2(K_{\mathrm{SD}}|\mathcal{A}|)\big)$. Compared with exhaustive ML detection, the proposed K-Best SD detector significantly reduces the search complexity and provides a flexible trade-off between detection performance and complexity by adjusting K_{SD}.

B. 2D-FFT-Based Sensing

Based on the sensing signal model in (6), we process the received echo in the frequency domain, where the target delay and Doppler shift manifest as phase rotations along the frequency and time dimensions, respectively. After dividing out the transmitted signal, a low-complexity 2D-FFT-based method is employed to estimate the target range and velocity. Under this framework, we further derive the range/velocity resolutions as well as the maximum unambiguous range/velocity.

Let $r_{\mathrm{F},m}[k]$ and $s_{\mathrm{F},m}[k]$ denote the frequency-domain representations of the received echo $r_{\mathrm{T},m}[n]$ and the transmitted signal $s_m[n]$, respectively, where $k = 0, 1, \ldots, N-1$ is the frequency index and $m = 0, 1, \ldots, N_{\mathrm{sym}} - 1$ is the nAFDM symbol index. Accordingly, the received frequency-domain echo can be expressed as

$$r_{\mathrm{F},m}[k] = s_{\mathrm{F},m}[k] G[k,m] + w_{\mathrm{F},m}[k], \tag{14}$$

where $w_{\mathrm{F},m}[k]$ is the frequency-domain noise and $G[k,m]$ is the sensing response over the frequency-time grid, given by $G[k,m] = \sum_{p=1}^{P_{\mathrm{s}}} \beta_p e^{-\imath 2\pi k \frac{\alpha}{T} \tau_p} e^{\imath 2\pi f_{D,p} m T_{\mathrm{sym}}}$.[1] The sensing response can be estimated by element-wise division as

$$D[k,m] = \frac{r_{\mathrm{F},m}[k]}{s_{\mathrm{F},m}[k]} = G[k,m] + \bar{w}_{\mathrm{F},m}[k], \tag{15}$$

where $\bar{w}_{\mathrm{F},m}[k] = w_{\mathrm{F},m}[k]/s_{\mathrm{F},m}[k]$ denotes the equivalent noise after division. By collecting $D[k,m]$ over N frequency samples and N_{sym} nAFDM symbols, an $N \times N_{\mathrm{sym}}$ sensing response matrix $\mathbf{D}$ is obtained. Then, a 2D-FFT operation is applied to estimate the range-Doppler profile. Specifically, an N-point inverse FFT (IFFT) is first performed along the frequency dimension to transform the frequency-dependent phase rotation into the delay domain, followed by an N_{sym}-point FFT along the time dimension to extract the Doppler information, yielding

$$\Gamma[b_r, b_v] = \sum_{m=0}^{N_{\mathrm{sym}}-1} \left(\frac{1}{N} \sum_{k=0}^{N-1} D[k,m] e^{\frac{\imath 2\pi k b_r}{N}} \right) e^{\frac{-\imath 2\pi m b_v}{N_{\mathrm{sym}}}}, \tag{16}$$

where $b_r = 0, 1, \ldots, N-1$ and $b_v = 0, 1, \ldots, N_{\mathrm{sym}} - 1$ denote the delay and Doppler indices, respectively. Accordingly, the normalized range-Doppler profile can be expressed as

$$\bar{\Gamma}[b_r, b_v] = \frac{|\Gamma[b_r, b_v]|}{\max_{b_r, b_v} |\Gamma[b_r, b_v]|}. \tag{17}$$

After applying FFT shift along the Doppler dimension, the target parameters can be estimated by searching for peaks in the normalized range-Doppler profile. In particular, the detected range-Doppler bins are obtained as

$$\{(\hat{b}_{r,p}, \hat{b}_{v,p})\}_{p=1}^{P_{\mathrm{s}}} = \mathrm{Peak}_{P_{\mathrm{s}}} \left\{ \bar{\Gamma}[b_r, b_v] \right\}, \tag{18}$$

where $\mathrm{Peak}_{P_{\mathrm{s}}}\{\cdot\}$ returns the locations of the P_{s} dominant peaks, with $\hat{b}_{r,p} \in [0, N-1]$ and $\hat{b}_{v,p} \in [-N_{\mathrm{sym}}/2, N_{\mathrm{sym}}/2 - 1]$ after FFT shifting. Next, the delay and Doppler estimates are given by $\hat{\tau}_p = \frac{T \hat{b}_{r,p}}{\alpha N}$ and $\hat{f}_{D,p} = \frac{\hat{b}_{v,p}}{N_{\mathrm{sym}} T_{\mathrm{sym}}}$. Accordingly, the range and velocity estimates can be calculated as

$$\begin{aligned} \hat{R}_p &= \frac{c\hat{\tau}_p}{2} = \frac{cT}{2\alpha N} \hat{b}_{r,p}, \\ \hat{v}_p &= \frac{c\hat{f}_{D,p}}{2f_c} = \frac{c}{2f_c N_{\mathrm{sym}} T_{\mathrm{sym}}} \hat{b}_{v,p}. \end{aligned} \tag{19}$$

Therefore, the range/velocity resolutions and the corresponding maximum unambiguous range/velocity are given

[1] As shown in (14), α directly affects the delay-dependent phase rotation along the frequency dimension, whereas it does not affect the Doppler-dependent phase rotation along the time dimension. Motivated by this separable frequency-time structure, a low-complexity 2D-FFT estimator is adopted in this work for range and velocity estimation. Developing advanced sensing algorithms specifically tailored to the non-orthogonal structure of nAFDM is an interesting direction and will be further explored in our future work.

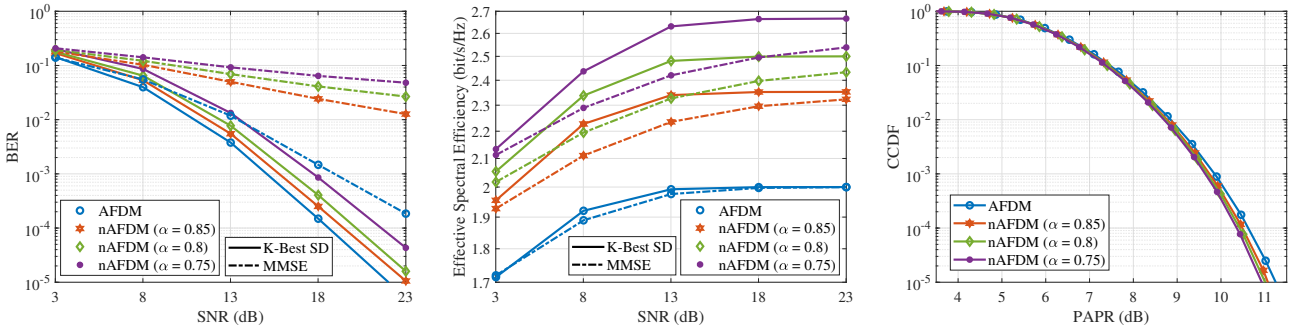

(a) BER (b) Effective SE (c) PAPR

Fig. 3. BER, effective SE, and PAPR performance of AFDM and nAFDM with $N = 64$, where the BER and effective SE are evaluated using the MMSE detector and the proposed K-Best SD detector with $K_{\mathrm{SD}} = 128$.

by

$$\Delta R = \frac{cT}{2\alpha N}, \quad R_{\max} = \frac{cT}{2\alpha},$$
$$\Delta v = \frac{c}{2f_c N_{\mathrm{sym}} T_{\mathrm{sym}}}, \quad v_{\max} = \frac{c}{4f_c T_{\mathrm{sym}}}. \tag{20}$$

This indicates that reducing α degrades the range resolution and increases the maximum unambiguous range, while both the velocity resolution and the maximum unambiguous velocity remain unchanged. Thus, α provides an additional sensing design degree of freedom that can be configured according to different range sensing requirements. Specifically, for a required range resolution ΔR_{req}, α should satisfy $\alpha \geq \frac{cT}{2N\Delta R_{\mathrm{req}}}$, whereas a maximum unambiguous range of at least R_{req} imposes $\alpha \leq \min\left(\frac{cT}{2R_{\mathrm{req}}}, 1\right)$.

For the 2D-FFT-based sensing algorithm, the element-wise division has a complexity of $\mathcal{O}(NN_{\mathrm{sym}})$. Moreover, the complexities of the N-point IFFT along the frequency dimension and the N_{sym}-point FFT along the time dimension are $\mathcal{O}(N_{\mathrm{sym}} N \log_2 N)$ and $\mathcal{O}(NN_{\mathrm{sym}} \log_2 N_{\mathrm{sym}})$, respectively. Therefore, the overall complexity of the 2D-FFT-based sensing algorithm can be expressed as $\mathcal{O}(NN_{\mathrm{sym}} (\log_2 N + \log_2 N_{\mathrm{sym}}))$.

IV. Simulation Results

In this section, we evaluate the communication and sensing performance of the proposed nAFDM-ISAC system. In all simulations, the carrier frequency is set to 77 GHz [8], QPSK modulation is adopted, and the chirp parameters are configured as $c_1 = c_2 = 5/(2N)$. In addition, AFDM and nAFDM employ the same symbol duration, i.e., $T = 5.12 \times 10^{-6}$ s. Accordingly, the subcarrier spacing is given by $1/T$ for AFDM and α/T for nAFDM.

A. Communication Performance

For the communication performance evaluation, the doubly selective channel consists of $P_{\mathrm{c}} = 3$ paths, with channel coefficients satisfying $h_{m,i} \sim \mathcal{CN}(0, 1/P_{\mathrm{c}})$. The maximum delay spread and normalized maximum Doppler shift are set to $l_{\max} = 2$ and $\nu_{\max} = 1$, respectively. The Doppler shift of each path follows Jakes' model, i.e., $\nu_{m,i} = \nu_{\max} \cos(\theta_{m,i})$, where $\theta_{m,i}$ is uniformly distributed over $[-\pi, \pi]$.

Fig. 3 shows the BER, effective SE, and PAPR performance of AFDM and nAFDM. To account for both the effect of bandwidth compression and the reliability penalty caused by non-orthogonality, the effective SE is defined as [14]

$$\eta_{\mathrm{eff}} = (1 - P_b)\frac{\log_2 M}{\alpha}, \tag{21}$$

where P_b denotes the BER and M is the modulation order. Here, $\log_2 M/\alpha$ represents the nominal SE enabled by bandwidth compression, while $(1 - P_b)$ indicates the probability of correctly detected bits. The BER and effective SE are evaluated using the MMSE detector and the proposed K-Best SD detector with $K_{\mathrm{SD}} = 128$. As shown in Fig. 3(a), the proposed K-Best SD detector consistently outperforms the MMSE detector for both AFDM and nAFDM. For nAFDM, the BER degrades as α decreases due to stronger non-orthogonality-induced interference. Fig. 3(b) presents the corresponding effective SE performance. As expected, nAFDM achieves a clear SE gain over AFDM, and the gain increases as α decreases. With the proposed K-Best SD detector, the effective SE of AFDM in the high signal-to-noise ratio (SNR) region is approximately 2.0 bit/s/Hz, while that of nAFDM with $\alpha = 0.85$, 0.8, and 0.75 reaches about 2.35, 2.50, and 2.67 bit/s/Hz, respectively. These values correspond to approximate effective SE gains of 17.65%, 25%, and 33.33% over AFDM. It should be noted that these effective SE gains already account for the BER penalty, rather than representing reliability-free net gains. Fig. 3(c) further compares the complementary cumulative distribution function (CCDF) of the PAPR for AFDM and nAFDM. It can be observed that nAFDM exhibits a slightly lower PAPR than AFDM, and this reduction becomes more pronounced as α decreases.

B. Sensing Performance

Fig. 4 illustrates the zero-Doppler and zero-delay cuts of the normalized ambiguity functions for AFDM and nAFDM with $N = 64$. As shown in Fig. 4(a), AFDM exhibits the narrowest delay mainlobe, while the mainlobe

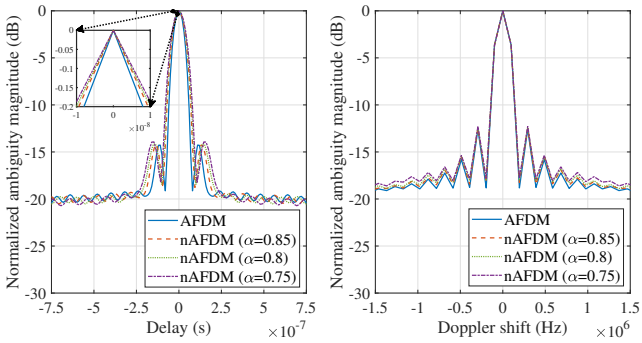

(a) Zero-Doppler cut (b) Zero-delay cut

Fig. 4. Zero-Doppler and zero-delay cuts of the normalized ambiguity functions for AFDM and nAFDM with $N = 64$.

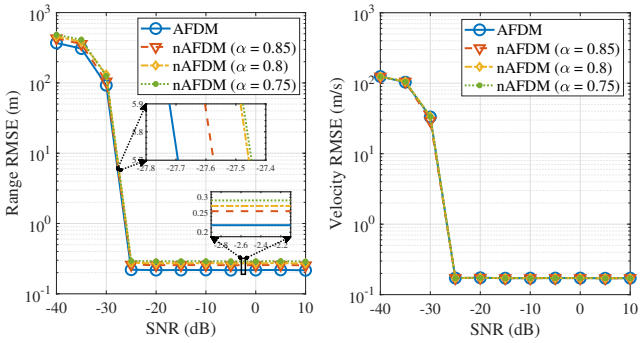

(a) Range RMSE (b) Velocity RMSE

Fig. 5. Range and velocity RMSE performance of AFDM and nAFDM.

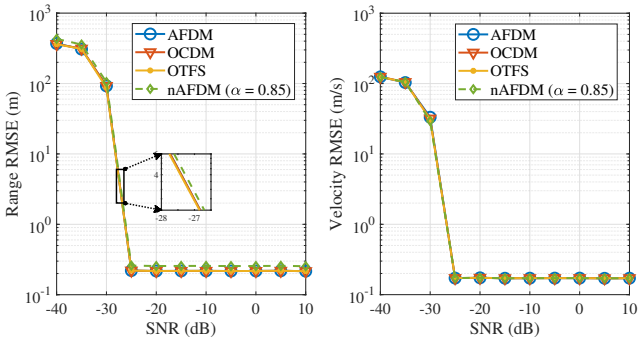

(a) Range RMSE (b) Velocity RMSE

Fig. 6. Range and velocity RMSE performance of AFDM, OCDM, OTFS, and nAFDM.

of nAFDM becomes slightly wider as α decreases. Since the delay resolution is inversely proportional to the signal bandwidth, this behavior can be attributed to the reduced bandwidth in nAFDM. By contrast, Fig. 4(b) shows that the Doppler cuts of AFDM and nAFDM almost overlap, and the corresponding mainlobe widths remain nearly unchanged for different values of α. This is because AFDM and nAFDM have the same symbol duration. The above results indicate that the bandwidth compression in nAFDM mainly degrades the delay resolution while having a negligible effect on the Doppler resolution.

Fig. 5 shows the range and velocity root mean square error (RMSE) performance of AFDM and nAFDM. Unless otherwise specified, all subsequent simulations are conducted with $N = 1024$, $N_{\text{sym}} = 512$, and $P_{\text{s}} = 1$. The range and velocity RMSE results are obtained from 50,000 Monte Carlo trials. In each trial, the target range and velocity are uniformly distributed over $[0.75, 192]$ m and $[0.59, 151.6]$ m/s, respectively. It can be seen from Fig. 5(a) that AFDM achieves the lowest range RMSE, while nAFDM exhibits a slight degradation that becomes more pronounced as α decreases because of the bandwidth compression in nAFDM. By contrast, as depicted in Fig. 5(b), the velocity RMSE curves of AFDM and nAFDM are nearly identical for all considered values of α, indicating that the impact of bandwidth compression on velocity estimation is marginal.

Fig. 6 compares the range and velocity RMSE performance of AFDM, OCDM, OTFS, and nAFDM. It can be observed from Fig. 6(a) that AFDM, OCDM, and OTFS achieve very similar range RMSE performance, while nAFDM with $\alpha = 0.85$ shows a moderately higher range RMSE owing to its reduced signal bandwidth. In Fig. 6(b), the velocity RMSE curves of all considered waveforms nearly overlap, since the velocity resolution is mainly determined by the symbol duration, which remains the same for the considered waveforms.

The analytical expressions in (20), together with the numerical results in Figs. 3–5, provide general insights for selecting α under different communication and sensing requirements. In particular, a smaller α is more suitable when higher effective SE and a larger sensing range are prioritized, whereas a larger α is preferable when higher communication reliability and range estimation accuracy are required.

V. Conclusion

In this paper, we have proposed a novel nAFDM-ISAC framework to simultaneously support spectrally efficient high-mobility communications and target sensing. We have developed a K-Best SD algorithm for communication detection by exploiting the AF-domain noise covariance matrix. For sensing, we have analytically derived the corresponding range and velocity resolutions, as well as the maximum unambiguous range and velocity, under the 2D-FFT-based sensing scheme. Numerical results have shown that nAFDM achieves a favorable trade-off among BER, effective SE, PAPR, and range and velocity estimation accuracy compared with conventional AFDM, and is a promising waveform for future ISAC systems.

References

[1] P. Yang, Y. Xiao, M. Xiao, and S. Li, "6G wireless communications: Vision and potential techniques," IEEE Netw., vol. 33, no. 4, pp. 70–75, Jul. 2019.

[2] X. Ouyang and J. Zhao, "Orthogonal chirp division multiplexing," IEEE Trans. Commun., vol. 64, no. 9, pp. 3946–3957, Sep. 2016.

[3] R. Hadani, S. Rakib, M. Tsatsanis, A. Monk, A. J. Goldsmith, A. F. Molisch, and R. Calderbank, "Orthogonal time frequency space modulation," in Proc. IEEE Wireless Commun. Netw. Conf. (WCNC), San Francisco, CA, USA, Mar. 2017, pp. 1–6.

[4] A. Bemani, N. Ksairi, and M. Kountouris, "Affine frequency division multiplexing for next generation wireless communications," IEEE Trans. Wireless Commun., vol. 22, no. 11, pp. 8214–8229, Nov. 2023.

[5] Y. Tao, M. Wen, Y. Ge, J. Li, E. Başar, and N. Al-Dhahir, "Affine frequency division multiplexing with index modulation: Full diversity condition, performance analysis, and low-complexity detection," IEEE J. Sel. Areas Commun., vol. 43, no. 4, pp. 1041–1055, Apr. 2025.

[6] Y. Tao, M. Wen, Y. Ge, T. Mao, Y. Tang, and A. Doosti-Aref, "Affine frequency division multiple access based on DAFT spreading for next-generation wireless networks," IEEE Trans. Wireless Commun., vol. 25, pp. 4626–4641, 2026.

[7] F. Liu, C. Masouros, A. P. Petropulu, H. Griffiths, and L. Hanzo, "Joint radar and communication design: Applications, state-of-the-art, and the road ahead," IEEE Trans. Commun., vol. 68, no. 6, pp. 3834–3862, Jun. 2020.

[8] Z. Gao et al., "Integrated sensing and communication with mmWave massive MIMO: A compressed sampling perspective," IEEE Trans. Wireless Commun., vol. 22, no. 3, pp. 1745–1762, Mar. 2023.

[9] A. Bemani, N. Ksairi, and M. Kountouris, "Integrated sensing and communications with affine frequency division multiplexing," IEEE Wireless Commun. Lett., vol. 13, no. 5, pp. 1255–1259, May 2024.

[10] F. Zhang et al., "AFDM-enabled integrated sensing and communication: Theoretical framework and pilot design," IEEE J. Sel. Areas Commun., vol. 44, pp. 310–324, 2026.

[11] Y. Zhang, Q. Yi, L. Musavian, T. Xu, and Z. Liu, "Non-orthogonal AFDM: A promising spectrally efficient waveform for 6G high-mobility communications," in Proc. IEEE 36th Int. Symp. Pers., Indoor Mobile Radio Commun. (PIMRC), Istanbul, Turkey, Sep. 2025, pp. 1–6.

[12] Q. Yi, Z. Liu, L. Musavian, and Z. Sui, "Non-orthogonal affine frequency division multiplexing for spectrally efficient high-mobility communications," IEEE Trans. Wireless Commun., vol. 25, pp. 15758–15774, 2026.

[13] C.-A. Shen and A. M. Eltawil, "A radius adaptive K-best decoder with early termination: Algorithm and VLSI architecture," IEEE Trans. Circuits Syst. I, Reg. Papers, vol. 57, no. 9, pp. 2476–2486, Sep. 2010.

[14] T. Xu, C. Masouros, and I. Darwazeh, "Design and prototyping of hybrid analog-digital multiuser MIMO beamforming for nonorthogonal signals," IEEE Internet Things J., vol. 7, no. 3, pp. 1872–1883, Mar. 2020.